

# The Cosmic Web, Multi-Stream Flows, and Tessellations

Sergei Shandarin,<sup>1</sup> Salman Habib,<sup>2</sup> and Katrin Heitmann<sup>2</sup>

<sup>1</sup>*Department of Physics and Astronomy, University of Kansas, Lawrence, KS 66045*

<sup>2</sup>*High Energy Physics Division, Argonne National Laboratory, Lemont, IL 60439*

(Dated: October 14, 2018)

Understanding the structure of the matter distribution in the Universe due to the action of the gravitational instability – the cosmic web – is complicated by lack of direct analytic access to the nonlinear domain of structure formation. Here, we suggest and apply a novel tessellation method designed for cold dark matter (CDM) N-body cosmological simulations. The method is based on the fact that the initial CDM state can be described by a 3-D manifold (in a 6-D phase space) that remains continuous under evolution. Our technique uses the full phase space information and has no free parameters; it can be used to compute multi-stream and density fields, the main focus of this paper. Using a large-box  $\Lambda$ CDM simulation we carry out a variety of initial analyses with the technique. These include studying the correlation between multi-streaming and density, the identification of structures such as Zel’dovich pancakes and voids, and statistical measurements of quantities such as the volume fraction as a function of the number of streams – where we find a remarkable scaling relation. Cosmological implications are briefly discussed.

PACS numbers:

## I. INTRODUCTION

The large-scale structure of the universe observed in modern redshift surveys like the 2dF Galaxy Redshift Survey and the Sloan Digital Sky Survey displays a complicated geometry – the ‘cosmic web’ – characterized by the presence of highly anisotropic concentrations of galaxies known as filaments. Another conspicuous feature of the large-scale structure is the presence of very large regions practically devoid of bright galaxies that are conventionally called ‘voids’. The filaments appear to be connected in a single percolating network, often with clusters of galaxies positioned at the nodal points. This complex structure is predicted by cosmological N-body simulations, which yield a very similar distribution in both dark matter halos that function as galactic hosts as well as in the dark matter density field itself.

Because of the essential role of nonlinearity, cosmological N-body simulations have become essential tools for studies of the formation and properties of the cosmic web. Collisionless gravity-only N-body simulations can yield high-resolution information regarding the distribution of matter and of dark matter-dominated halos. A first principles approach to galaxy formation, however, requires a full treatment of gas physics and processes such as star formation and feedback from supernovae and AGN. Because of the difficulty of this second step, analysis of observations is mostly performed by using a phenomenological approach on top of gravity-only simulations. Thus galaxies may be added to such simulations using halo occupation distributions or semi-analytic models. Nevertheless, density fields created from the particle or halo distributions can be useful for morphological analyses of the formed large-scale structures (see e.g., Refs. [1–3]).

Several different approaches exist to estimate density

fields from a particle distribution; many different methods have been suggested for implementing these estimators. More than a dozen have been discussed and compared in recent publications [4–6]. These methods can be conveniently divided into two classes: those that employ a tessellation of space e.g., the Delaunay Tessellation Field Estimator (DTFE) [1, 3, 7], and those that use particle-deposition in some form e.g., Cloud-In-Cell (CIC) [8] or the Smooth Particle Hydrodynamics (SPH) method [9, 10]. Here, we suggest a new approach based on tessellation, that to our knowledge, has not been previously used in cosmology.

Most density estimation methods use only the particle position information; these are therefore limited to studies confined to configuration space. However, incorporating particle velocities – easily available in cosmological N-body simulations – into the analysis allows one to probe the full phase space, potentially greatly advancing the understanding of the dynamics and morphology of the cosmic web [6, 11, 12].

Here we suggest the incorporation of dynamical information by using the initial positions of the simulation particles together with the final positions, in contrast to using the phase space information available only at the final stage of the evolution. It is possible to do this in CDM-based models of structure formation because the initial condition is specified with a self-consistently determined vectorial velocity field, uniquely defined at each spatial point.

In a classical Hamiltonian system, the initial coordinates and momenta completely determine the path of the system in phase space. However, it is well known that canonical transformations allow great freedom in choosing generalized coordinates and momenta [13]. One particular choice is to use the initial and final coordinates instead of the initial coordinates and initial velocities,

since both sets completely define the path of the system in phase space. Therefore, the set of the initial and final coordinates contains the same dynamical information as the phase space information at the initial or final time. Although this information is sufficient for the determination of the phase space trajectory, it obviously has a very different form. Therefore, the analysis must proceed along different lines than those pursued in previous phase space-based studies (Refs. [6] or [11]).

It is important to emphasize that the (tracer) particles in a cosmological N-body simulation have no intrinsic physical meaning. The choice of their sizes and masses is dictated by computational considerations alone. The physical equivalents of particles in N-body simulations would be clouds of huge sizes, volumes, and numbers of physical particles such as neutralinos or axions. These clouds are certainly not rigid bodies nor uniform formations. In the real world, at the initial stage of a simulation, they might be the structures qualitatively similar to the final stage of the simulation but significantly smaller in scale. It is well known that their overall shape evolves: some get squeezed, others expand, and the shape deformation is highly anisotropic, see e.g., Ref. [14]. Thus, using rigid particles in simulations is just a computationally efficient technique to approximate the physical evolution of collisionless self-gravitating systems.

The first major assumption in our approach is that the mass is not concentrated in the form of a hard voxel around each point but is relatively uniformly spread between the points. A typical particle realization of an initially uniform mass distribution is to assign the particles to the nodal points of a cubic grid (‘quiet start’). In simulations, the initial position and velocity perturbations are implemented by applying the Zel’dovich approximation (or a higher-order Lagrangian approximation) to this initial set of points. In our case, the nodes of the cubic grid are interpreted as the vertices of a set of tetrahedra that tile the space (at the initial stage) without holes or other defects. This is the initial tessellation of Lagrangian space.

The particles are then evolved using a standard N-body code. The important difference compared to other approaches using tessellations – in most cases the Voronoi or Delaunay tessellations – is that the initial tessellation remains intact, preserving its initial neighbor structure. Consequently, the 3-D hypersurface describing the initial state of the system in 6-D phase space remains continuous and the tetrahedra completely tile it at any stage of the evolution. In 3-D configuration space, however, the tetrahedra can overlap significantly, turn inside out, get squeezed, or expand without limits. In order to estimate the density from the tessellation, we have to make a second major assumption: the tetrahedra must remain uniform. Without knowledge of the structures on subgrid scales, this seems to be the only sensible assumption. It sets the physical limit to the maximum spatial resolution of the density and other fields.

Thus, in our approach we use the tessellation of La-

grangian (initial) space and map it to Eulerian (final) space using the results of an N-body simulation. As described below, our tessellation of Lagrangian space is neither of the Voronoi nor of the Delaunay kind. It’s one point of similarity with Delaunay tessellation is that it tiles Lagrangian space using tetrahedra with particles at the vertices. The tessellation represents a continuous 3-D manifold in 6-D phase space. Because of the symplectic nature of the underlying evolution, the mapping to Eulerian space is continuous, and the manifold remains three-dimensional and continuous despite the fact that it folds in extremely complex ways during the nonlinear stages of the evolution. The continuity of the manifold allows us to identify multi-stream flows and to count streams, as well as estimate other fields at an arbitrary point of Eulerian space.

The paper is organized as follows: we start with the description of the tessellation we use and then explain how to compute the number of streams and the density at an arbitrary point at a chosen instant of time. For illustrative purposes, we then compare the particle distribution and the multi-stream and density fields in a small box cut out from the full N-body simulation of a  $\Lambda$ CDM cosmology. After this, we present a statistical analysis of the tetrahedra parameters at the nonlinear stage. We find the probability distribution function (pdf) of the multi-stream field and density fields in regions with constant number of streams and discuss their properties. Finally, we discuss cosmological implications and summarize the results.

## II. TESSELLATIONS VS. PARTICLES

The central aim of this work is to explore the prospects of using multi-stream flows for better understanding the nonlinear regime of the gravitational instability and the structure of the basic elements of the cosmic web i.e., clumps, filaments, pancakes, and voids, as suggested in Ref. [15]. We will describe a novel technique of probing the multi-stream flows based on tessellation of the 3-D manifold in 6-D phase space describing the evolution of a cold collisionless medium – significantly superior to the one used in Ref. [15].

Figure 1 provides a 2-D toy model illustration of the main differences between using particles and tessellations. We begin with considering Lagrangian space, the common starting point for generating initial perturbations in positions and velocities of particles in cosmological N-body simulations [16–18]. The homogeneous state is approximated by generating a regular square mesh with particles placed at the nodes as shown in the top left panel. The ensuing evolution of the system is completely described by the motion of the particles. The particles can be assigned sizes as illustrated by a CIC example in the bottom left panel.

Alternatively, the nodes of the initial mesh can be considered as the vertices of a triangular tessellation as

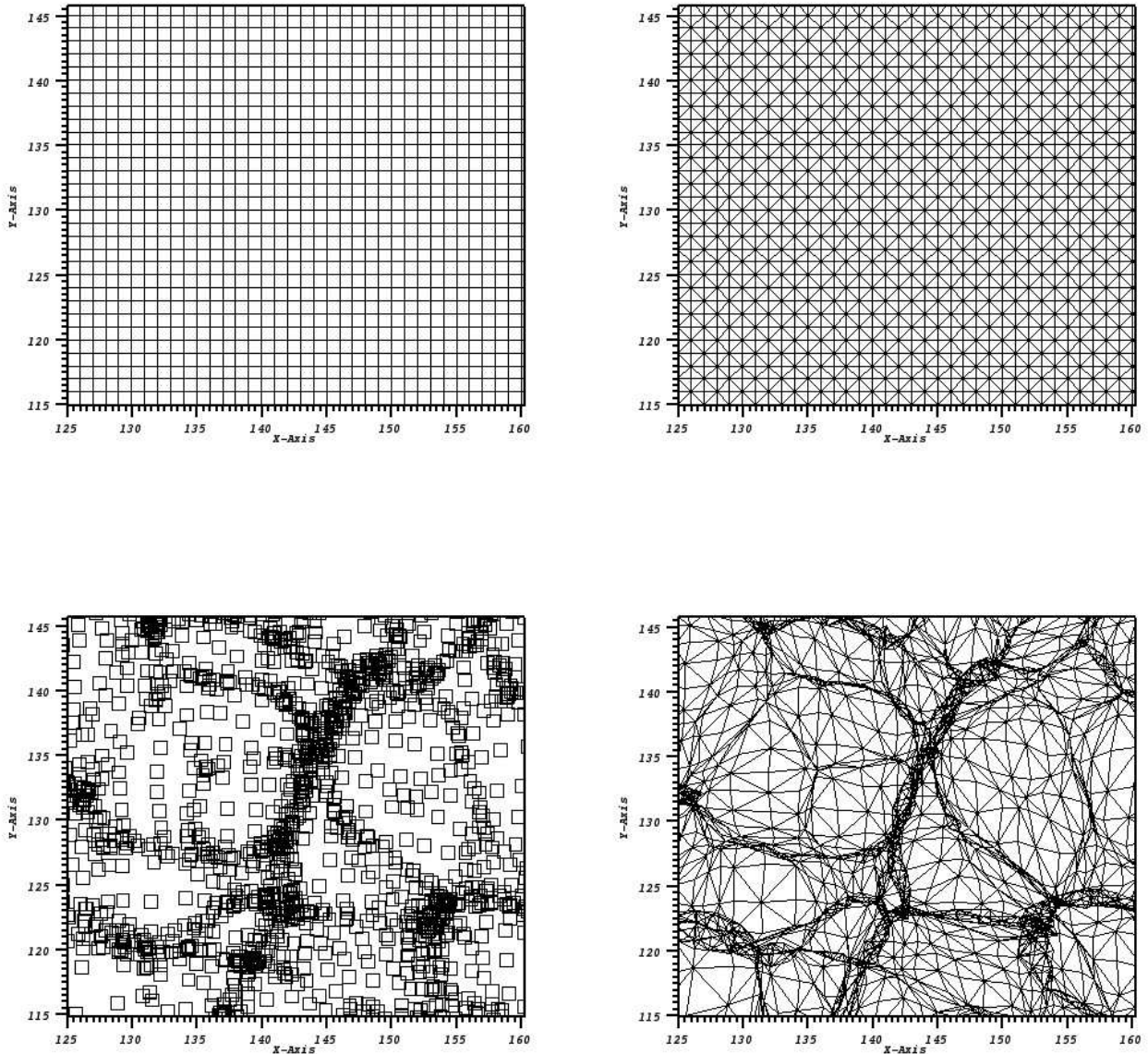


FIG. 1: Two-dimensional illustration of the difference in representing density fields by using particles (left column) and tessellations (right column). The top panels exhibit Lagrangian space where the density is uniform while the bottom panels display the system at a nonlinear stage of the evolution. The nodes of the triangulation in the right panel are at the positions of the particles in the left panel. The density field can be derived from the particle/node coordinates.

shown in the top right panel of Fig. 1. The motion of the particles/nodes results in the displacement of the triangles along with their deformation (bottom right panel). The bottom panels demonstrate the similarities as well as the main differences of the two approaches. The generic disadvantage of the CIC representation is related to two problems. First, structures smaller than the ‘particle size’ are filtered, and entirely empty regions can be pro-

duced that are unphysical in the context of dark matter dominated cosmological models. Adaptive gridding schemes can help alleviate these problems but do not completely eliminate them. In addition, they typically involve one or more free parameters. For our purposes, a tessellation approach is therefore more natural.

Now we turn to the case of 3-D space. As in the case of two dimensions, we start with a cubic mesh in La-

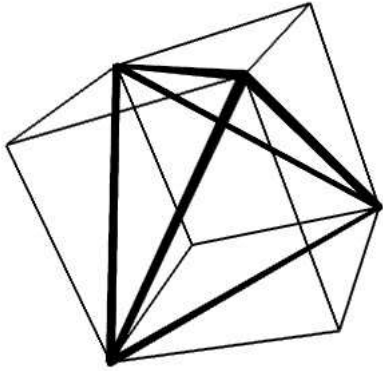


FIG. 2: Decomposition of a cube into five tetrahedra. The central tetrahedron shown by a heavy line is regular and its volume equals a third of the volume of the cube. Each of the remaining four tetrahedra is half of the volume of the central one, or one-sixth of the volume of the cube.

grangian space and place particles at the nodes of the mesh. Then we decompose each elementary cube into several tetrahedra as shown in Fig. 2. The goal is to tessellate a continuous 3-D manifold or hypersurface in a 6-D phase space without holes or other defects. This requires that the faces and edges of the adjacent tetrahedra must match to each other. In order to achieve this goal, the adjacent cubes that have a common face must be rotated by 90 degrees with respect to each other. It is worth stressing that the tessellation employs only particles i.e., the nodes of the Lagrangian tessellation. This guarantees that during further manipulations we will use only information contained in the positions and velocities of the particles. Out of several possible options we have chosen to decompose the fundamental cube into five tetrahedra as shown in Fig. 2. A minor disadvantage of this choice is the presence of two kinds of tetrahedra differing in their shapes and volumes.

The advantages of using tessellations – in particular Voronoi and Delaunay tessellations – for studying the cosmic web have been investigated and described in detail by van de Weygaert and collaborators (see e.g., Refs. [1, 3, 19, 20] and references therein). We repeat that the tessellation we use here is neither of the Voronoi nor Delaunay type. The only analogy of our tessellation with the Delaunay tessellation is that both are 3-D triangulations – as all elements of the tessellation are tetrahedra. We also wish to stress another key difference: we build our tessellation only once in Lagrangian space. In the dynamical evolution that follows, the same sets of nodes define each tetrahedron as in Lagrangian space. As a result, the neighboring tetrahedra always share the same faces, edges, and vertices. The tetrahedra may arbitrarily change their sizes, be turned inside out many times and overlap in the course of the evolution of the system, but the initial 3-D manifold remains continuous.

Preserving continuity of the 3-D manifold allows us to identify multi-stream flows and easily count streams at arbitrary points in Eulerian space.

### III. COMPUTING MULTI-STREAM AND DENSITY FIELDS FROM THE TESSELLATION

The nonlinear stage of gravitational instability in a collisionless CDM model is characterized by the emergence of regions where more than one stream (or flow) can coexist at the same point in space. Zel'dovich [21] was the first to discuss this phenomenon in the context of the formation of structure in the Universe. In particular, Zel'dovich predicted the formation of very oblate concentrations of mass which he baptized as ‘pancakes’. The pancakes are the first unambiguously nonlinear structures to grow from generic initial density fluctuations in a continuous cold medium under the action of gravity, see e.g., Ref. [22].

#### A. Multi-stream field

We define a multi-stream field as a field taking discrete values that are equal to the number of streams at every evaluation point. At a generic point the number of streams is always an odd integer. An even number of streams occurs only on caustic surfaces i.e., on a set of zero volume. As the nonlinear stage progresses, the three-dimensional manifold becomes more wrapped and folded in phase space, especially in the regions of high density such as dark matter halos, where the dynamical timescale is short. When a new fold emerges, the number of streams increases by two at every point in the region of the newly formed fold. The formation of new streams indicates the advance of nonlinearity and therefore the multi-stream field is an objective quantitative characteristic of nonlinear evolution [15].

A typical local characteristic of nonlinearity in cosmological studies is simply the density. The root mean square deviation of density,  $\sigma_\delta = \langle \delta^2 \rangle^{1/2}$ , where  $\delta \equiv (\rho - \bar{\rho})/\bar{\rho}$ , is commonly used as a global characteristic of nonlinearity. While the virial overdensity factor value of  $\sim 200$  is grounded in the dynamics of halos, in general the value of  $\sigma_\delta$  has a rather vague relation to the complex dynamics that occurs between the linear stage and the virial equilibration of halos. It appears that the multi-stream field can describe some aspects of nonlinearity differently – and sometimes better – than the density, especially in pancakes and filaments [15].

If the tessellation of the volume occupied by the system is established in the homogeneous state or the linear regime, then one can compute the multi-stream field at any time from the current coordinates of the particles without following their trajectories. Let us consider an arbitrary point in Eulerian space. The number of streams at this point is equal to the total number of tetrahedra

for which the chosen point is internal. Whether a chosen point is inside or outside a tetrahedron can be established by computing five determinants as described below.

If the coordinates of the chosen point are  $(x, y, z)$ , and the vertices of a certain tetrahedron have the coordinates  $(x_i, y_i, z_i)$  ( $i = 1, 2, 3, 4$ ), then the determinant computed using the coordinates of the vertices

$$d_0 = \begin{vmatrix} x_1 & y_1 & z_1 & 1 \\ x_2 & y_2 & z_2 & 1 \\ x_3 & y_3 & z_3 & 1 \\ x_4 & y_4 & z_4 & 1 \end{vmatrix} \quad (1)$$

and four determinants that also use the coordinates of the point itself

$$d_1 = \begin{vmatrix} x & y & z & 1 \\ x_2 & y_2 & z_2 & 1 \\ x_3 & y_3 & z_3 & 1 \\ x_4 & y_4 & z_4 & 1 \end{vmatrix}, \quad d_2 = \begin{vmatrix} x_1 & y_1 & z_1 & 1 \\ x & y & z & 1 \\ x_3 & y_3 & z_3 & 1 \\ x_4 & y_4 & z_4 & 1 \end{vmatrix},$$

$$d_3 = \begin{vmatrix} x_1 & y_1 & z_1 & 1 \\ x_2 & y_2 & z_2 & 1 \\ x & y & z & 1 \\ x_4 & y_4 & z_4 & 1 \end{vmatrix}, \quad d_4 = \begin{vmatrix} x_1 & y_1 & z_1 & 1 \\ x_2 & y_2 & z_2 & 1 \\ x_3 & y_3 & z_3 & 1 \\ x & y & z & 1 \end{vmatrix} \quad (2)$$

all have the same sign, then the point is inside the tetrahedron. The determinant  $d_0$  also gives the volume of the tetrahedron  $V = |d_0|/6$ . If  $d_0 = 0$ , then four vertices of the tetrahedron are coplanar and its volume is zero. If  $d_0 < 0$ , then it has turned inside out an odd number of times. If any other  $d_i = 0$  ( $i = 1, 2, 3, 4$ ), then the point lies on the face  $i$  which is opposite to the vertex  $i$ . If the sign of  $d_i$  is different from that of  $d_0$ , then the point lies outside the boundary of face  $i$ , otherwise it is inside. Formally the multi-stream field can be computed with arbitrary resolution, however, the real physical accuracy of such a computation is ultimately determined by the mass and force resolution of the simulation.

## B. Density field

The method for computing the multi-stream field can be easily extended for computing the density. After finding that a point resides inside a particular tetrahedron, one can compute the volume of the tetrahedron, and therefore the associated density, assuming that the mass within every tetrahedron is conserved and its density is uniformly distributed. Summing up the densities over all streams one finds the density at the chosen point. As in the case of the multi-stream field the density field can be computed on an arbitrary mesh or on an arbitrary irregular set of points.

## IV. MULTI-STREAM FIELD IN $\Lambda$ CDM

We now apply the technique described above to study aspects of the large-scale structure in a standard  $\Lambda$ CDM

cosmology. Because our main aim here is to introduce the technique, we restrict ourselves to a relatively small number of illustrative examples.

### A. The cosmological model and simulation parameters

The formation of structure is modeled here by a gravity-only N-body simulation in a  $512h^{-1}$ Mpc-sided cubic box using the HACC (Hardware Accelerated Cosmology Code) framework [23, 24] in its medium-resolution, particle-mesh (PM) mode. The number of particles is  $512^3$  and the grid size in the gravitational Poisson solver is  $1024^3$ . The parameters of the  $\Lambda$ CDM cosmological model are as follows:  $h = H_0/(100 \text{ km/s} \cdot \text{Mpc}) = 0.72$ ,  $\Omega_{tot} = 0.25$ ,  $\Omega_b = 0.043$ ,  $n = 0.97$ ,  $\sigma_8 = 0.8$ , the initial redshift  $z_{in} = 200$ . These parameter values are roughly consistent with current measurements; our aim here is not to test the standard cosmological model but to provide a more or less realistic environment within which to try out the new technique. For ease of analysis, in the following we will restrict ourselves to a relatively modest spatial dynamic range (hence the choice of the HACC PM mode made here). Analysis of high-resolution HACC simulations will be reserved for a later publication.

### B. Small box study

We first demonstrate our new method by studying a small cubic box cut out from the main simulation volume described above. The size of the small box is  $8h^{-1}$ Mpc. We shall see later that there are several pancakes in this box and that they form a quite complicated structure; even at this relatively small scale, they overlap in projection, obstructing the structures behind them. Because of this problem, structure in a box of significantly greater size becomes difficult to visualize. Hence, it is useful to first use a small box to illustrate the properties of our method.

The mean density in the chosen box is  $\rho_{\text{box}} = 1.78\bar{\rho}$  where  $\bar{\rho}$  is the mean density in the Universe. The total number of non-overlapping boxes of this size in the simulation volume is  $64^3 = 262144$ ; this allows us to obtain quite accurate statistics describing the regions of this shape and size. The Universe is highly inhomogeneous on the box scale. The mass, and therefore mean density,  $\rho_{\text{box}}$ , of the boxes have a highly nongaussian pdf as can be seen from the following numbers:  $\min(\rho_{\text{box}}) = 0.043\bar{\rho}$ ,  $\text{median}(\rho_{\text{box}}) = 0.62\bar{\rho}$ ,  $\langle \rho_{\text{box}} \rangle = \bar{\rho}$ ,  $\text{std}(\rho_{\text{box}}) = 1.32\bar{\rho}$ , and  $\max(\rho_{\text{box}}) = 61.7\bar{\rho}$ . The chosen box contains roughly 80% more particles than the average box with the same size (i.e., it is roughly 80% more massive). About 13% of such boxes, i.e., slightly more than 34,000 boxes overall, have greater masses.

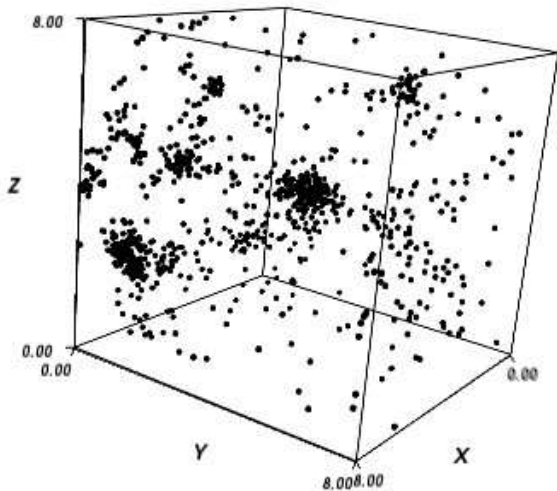


FIG. 3: Particle distribution i.e., tetrahedron vertices in a small sub-cube of size  $8h^{-1}\text{Mpc}$  extracted from the full simulation.

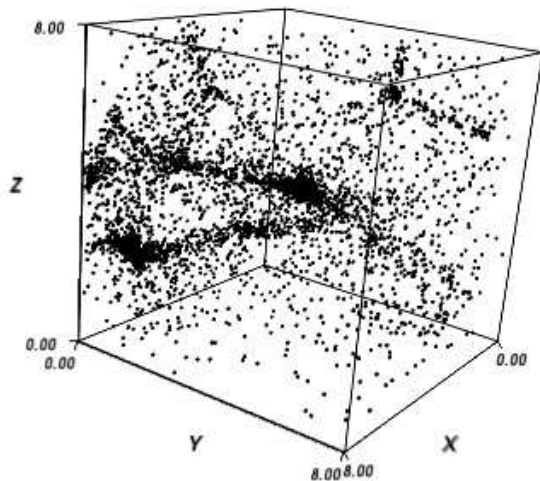


FIG. 4: Distribution of the tetrahedron centroids in the same region as in Fig. 3. The size of the dots is reduced in order to approximately compensate for the larger number of dots.

### 1. Vertices vs. tetrahedra centroids

We first compare the spatial distributions of particles (used as the vertices of the tetrahedra) with the distribution of the tetrahedra centroids. The coordinates of the centroids are easy to compute since they are simply the mean values of the vertex coordinates:  $\mathbf{x}_c = 1/4 \sum_{i=1}^4 \mathbf{x}_{v,i}$ . If the density in a tetrahedron is uniform then its centroid is also the center of mass of the

tetrahedron.

Figures 3 and 4 show the spatial distribution of the particles, i.e., vertices and centroids of the tetrahedra in the chosen box. The number of centroids is five times greater than that of the vertices since each elementary cube is decomposed into five tetrahedra. The visual comparison of the figures suggests that the distribution of centroids appears more filamentary than that of the vertices. It also hints at the presence of a few very thin sheets spanning the entire box. Unfortunately this can only be fully appreciated when the distribution is manipulated (e.g. rotated) with three-dimensional visualization software on a computer screen [36].

### 2. Density field vs multi-stream field

We now show the multi-stream and density fields computed using the tessellation method in Fig. 5 in the box depicted in Figs. 3 and 4. The overall parameters of the multi-stream field computed on a  $128^3$  uniformly-sampled grid are as follows:  $n_{s,\min} = 1$ ,  $n_{s,\text{med}} = 1$ ,  $\langle n_s \rangle = 1.45$ ,  $\text{std}(n_s) = 1.93$ ,  $n_{s,\max} = 141$ . The overall parameters of the density field within the selected box (also computed on a  $128^3$  grid) are as follows:  $\rho_{\min} = 0.032\bar{\rho}$ ,  $\rho_{\text{med}} = 0.16\bar{\rho}$ ,  $\langle \rho \rangle = 1.78\bar{\rho}$ ,  $\text{std}(\rho) = 38.5\bar{\rho}$ ,  $\rho_{\max} = 2.2 \times 10^4 \bar{\rho}$ , where  $\bar{\rho}$  is the mean density in the Universe and  $\langle \rho \rangle$  is the mean density within the chosen box.

Figure 5 demonstrates the crucial role of spatial resolution. The multi-stream and density fields computed with increasing resolution on sampling meshes with  $8^3$ ,  $32^3$  and  $128^3$  nodes are shown in the bottom and top panels respectively. It is remarkable that the three-stream flows clearly seen as a pancake in the multi-stream field in the bottom left panel at the lowest spatial resolution of  $1h^{-1}\text{Mpc}$  but not seen in the density field in top left panel. The filaments and pancakes appear in the middle column and acquire more details in the right column. This allows us to tentatively conclude that the pancakes and filaments in the box are thinner than  $\sim 1h^{-1}\text{Mpc}$  and some parts of the structure are even thinner than  $\sim 1/4h^{-1}\text{Mpc}$ .

As in the case of the multi-stream field, the density field clearly reveals structure in more detail as resolution is increased. Note that the multi-stream and density fields are not identical as stressed in Ref. [15]. The correspondence of the peaks in the density field to the clumps in the particle distribution in Fig. 3 is much stronger than that of the multi-stream field.

Figure 6 shows the distribution of densities in 1, 3, 5, 7, 9, 15, and 21-stream flow regions computed on the high resolution mesh with  $128^3$  nodes. The horizontal axis is the logarithm of the density. The vertical axis is the logarithm of the number of nodes in each of 32 equal logarithmic bins in the range of densities from  $\rho = 0.03\bar{\rho}$  to  $\rho = 3,000\bar{\rho}$ . The peak and the bulk of the distribution shift monotonically to higher densities as the number of

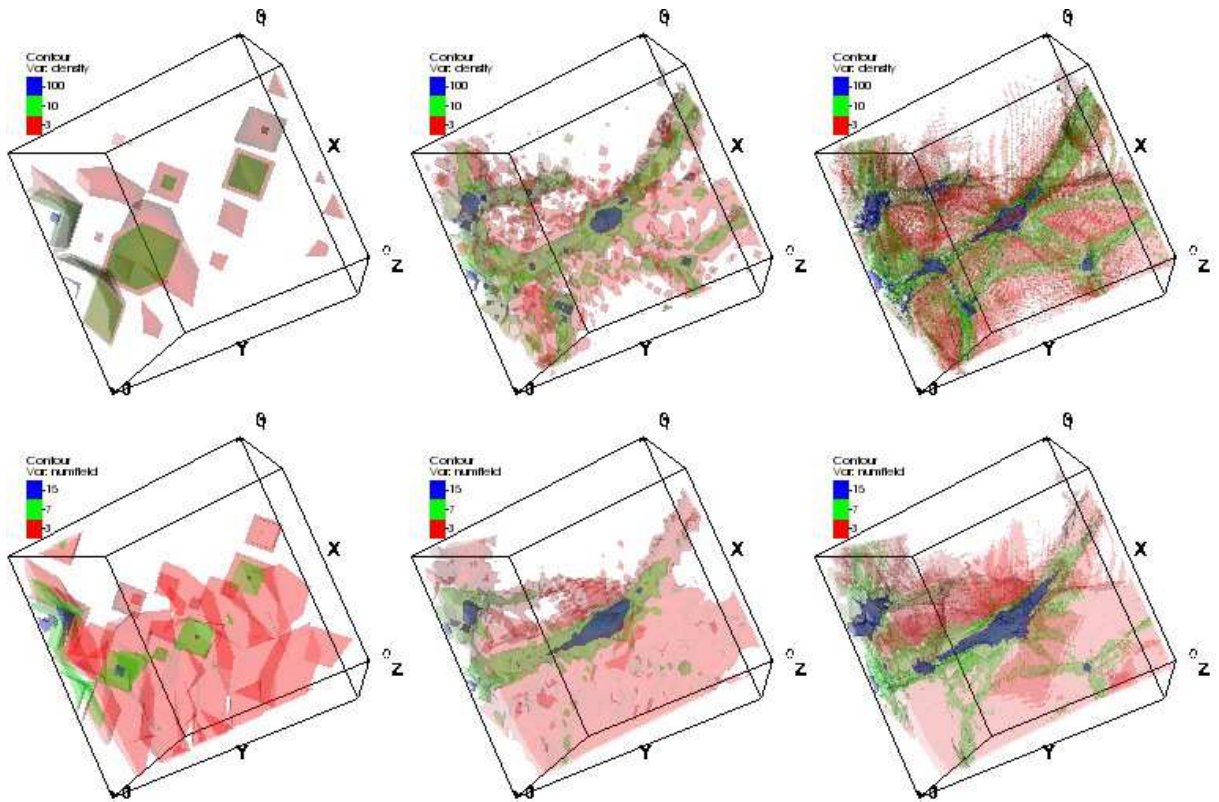


FIG. 5: Same box as in Figs. 3 and 4. The top and bottom panels show the density and multi-stream fields respectively. The fields in the left column are sampled on an  $8^3$  grid, in the middle column on a  $32^3$  grid, and in the right column on a  $128^3$  grid. The three density contours are:  $3\bar{\rho}$  – red,  $10\bar{\rho}$  – green, and  $100\bar{\rho}$  – blue, and the three multi-stream contours are: 3 – red, 7 – green, and 15 – blue. One can clearly see how filaments and pancakes emerge with increasing resolution from the left to right.

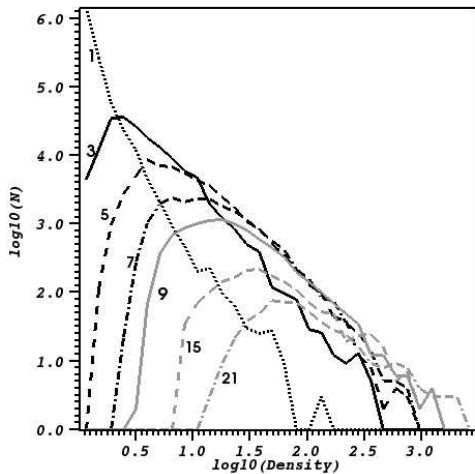


FIG. 6: Number of sampling mesh nodes as a function of density in the regions with number of streams shown next to each curve.

streams is increased; this is mostly due to the absence of low density sites in regions with high numbers of streams.

The dependence of the high end of the distribution on the number of streams is considerably weaker than that of the low end. The high end of the distribution appears to converge to an envelope with a simple power law  $N \propto \rho^{-1.45}$ . We will show later below that although this kind of trend is qualitatively similar in a much larger box (of size  $384h^{-1}\text{Mpc}$ ), the slope of the power law envelope is significantly steeper. This is a clear indication of large-scale bias.

### 3. High resolution density field vs particle distribution

Here we discuss how the high resolution density field is related to the spatial distribution of particles. In Fig. 7 we present four panels showing the density field and particle distribution. All four panels display the same density contour  $\rho/\bar{\rho} = 10$ . The particles in the panels are selected according to the number of streams at the position of each particle. The contour surface is semitransparent to allow us to see particles inside the contour. The top left panel shows only particles that reside in the regions with nine or greater number of streams; the total number of these particles is  $n_{\geq 9} = 338$ . All of them lie inside the density contour  $\rho/\bar{\rho} = 10$ , and they are concentrated

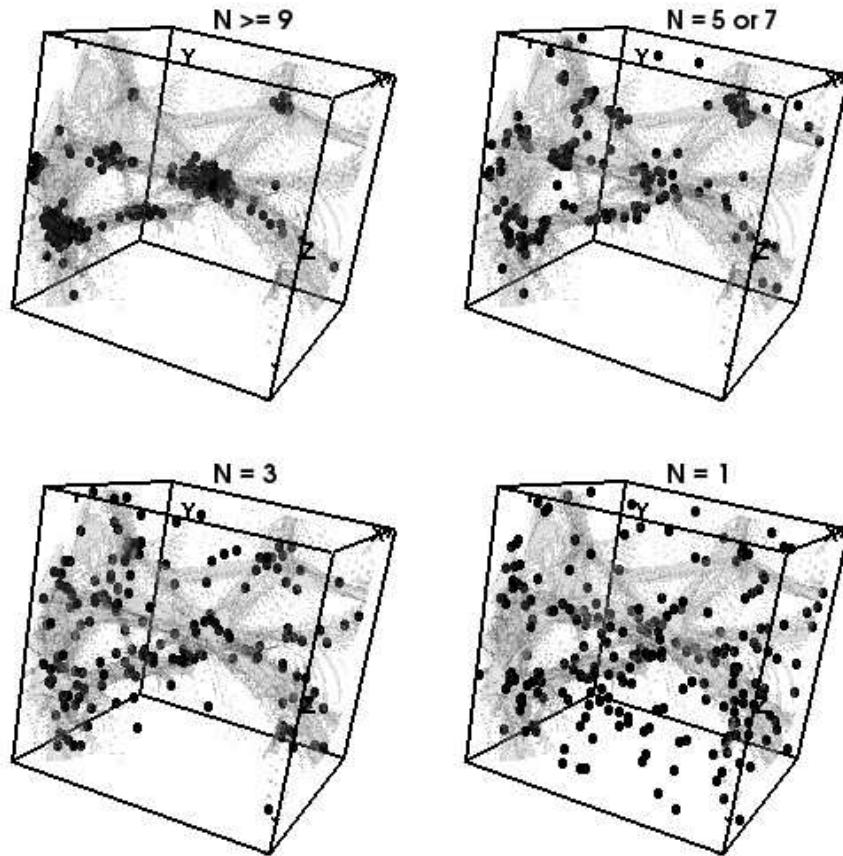


FIG. 7: Particles lying in regions with different numbers of streams vs density. The box is the same as in the previous figures. All four panels show the density contour  $\rho/\bar{\rho} = 10$ . The panels show particles lying in  $\geq 9$ -, 5- or 7-, 3-, and one-stream flows.

in the clumps located at the junctions of the filaments. The top right panel shows particles in five- and seven-stream flows, totalling  $n_5 + n_7 = 93 + 77 = 170$  particles. Practically all of these particles lie within the filaments except a few that are in pancakes. The bottom left panel shows  $n_3 = 185$  particles residing in the three-stream flows only. The chosen density level  $\rho/\bar{\rho} = 10$  shows only hints of pancakes and the chosen particles tend to be in those regions. Finally, the bottom right panel shows only particles ( $n_1 = 222$ ) located in the regions with only one stream i.e., in voids. A closer inspection shows that no single particle lies inside the chosen density contour. (Unfortunately the projection effect in the figure does not allow one to appreciate this to the full.) The figure and these numbers are in qualitative agreement with Fig. 6: there is an obvious correlation between the multi-stream and density fields but there is not a one-to-one correspondence. It is worth being reminded that this particular box has a mass that is almost 80% greater than that expected on average. Therefore, the mass fractions in clumps, filaments, pancakes, and voids  $f_{m,c} : f_{m,f} : f_{m,p} : f_{m,v} \approx n_{\geq 9} : n_{7,5} : n_3 : n_1 \approx 37\%:18\%:20\%:24\%$  may not be necessarily typical. We stress that this estimate is based on a rough reading of Fig. 6, more reliable estimates will

require a morphological analysis that will be reported on in a separate paper.

## V. STATISTICS OF TETRAHEDRA PARAMETERS

In order to evaluate multi-stream, density or other fields using the tessellation one must make use of the tetrahedra that are principle elements of the tessellation. Their control over many properties of the derived field is considerably more elaborate than the type and size of the elements of a regular grid. Therefore it is worth examining some of their parameters in more detail. In the tessellation approach, the information stored in the particle coordinates is used to compute various parameters of the set of tetrahedra that are generated in Lagrangian space. The tetrahedra are arranged in a semi-regular mesh in Lagrangian space but after mapping to Eulerian space form an irregular partly overlapping mesh (see Fig. 1 for an illustration). All other fields, e.g., multi-stream and density fields, are derived from the parameters of the tetrahedra and therefore they are also specified on an irregular mesh. We have already described how the



multi-stream and density fields can be computed on a regular rectangular mesh of arbitrary sampling resolution, or on an arbitrary set of points. Here we study the statistics of the basic parameters of the tetrahedra. The complete description of an arbitrary tetrahedron requires six parameters (e.g., the lengths of all edges), thus the full description of the shapes requires a five-dimensional parametric space. We select only four parameters consisting of the tetrahedron volume and three others that characterize the shape. These ‘basic parameters’ will be defined and discussed further below. The statistics below are obtained using the results from the  $384h^{-1}\text{Mpc}$  box.

### A. Tetrahedra volumes

There are only two kinds of tetrahedra in the tessellation of Lagrangian space: ‘small’, with volume  $1/6$  and ‘large’, with volume  $1/3h^{-3}\text{Mpc}^3$  (see Fig. 2) for the simulation at hand, where the initial inter-particle separation is  $1h^{-1}\text{Mpc}$ . The large tetrahedron is regular with edges equal to  $\sqrt{2}h^{-1}\text{Mpc}$ . The smaller tetrahedron has three mutually orthogonal faces which are isosceles right triangles with catheti equal to  $1h^{-1}\text{Mpc}$  and the fourth face is an equilateral triangle with sides equal to  $\sqrt{2}h^{-1}\text{Mpc}$ . As the system evolves, the tetrahedra change their sizes and shapes.

At the nonlinear stage of the evolution, the volumes of most tetrahedra undergo many cycles of collapsing to zero followed by expansion. The volume of a tetrahedron can be easily computed from the coordinates of its vertices either by using Eq. (1) or the vector algebra expression. If three edges of a tetrahedron that meet at one vertex are represented by vectors  $\mathbf{a}$ ,  $\mathbf{b}$  and  $\mathbf{c}$ , then its volume is given by the scalar triple product

$$V = \frac{1}{6} \mathbf{a} \cdot \mathbf{b} \times \mathbf{c}. \quad (3)$$

The sign of the volume obviously depends on the mutual orientation of the vectors and can change in the course of evolution. The change of the sign of the volume in Eq. 3 indicates the formation or vanishing of caustic elements which are the common faces of the neighboring tetrahedra having volumes with opposite signs. As the volume changes continuously it must pass through zero at some instant of time – this can happen only when one vertex of a tetrahedron crosses the face formed by its other three vertices so that all four vertices of the tetrahedron instantaneously lie on a plane. Since this face also belongs to the neighboring tetrahedron the vertex that crossed the face now lies in the interior of the neighboring tetrahedron. Therefore the number of streams is increased in the overlapping part by two, because the vertex is also shared by several other tetrahedra that therefore also overlap with the neighboring tetrahedron. The three-dimensional hypersurface can be wrapped in an arbitrarily complex manner in six-dimensional phase space but it must never be torn, nor ever intersect itself.

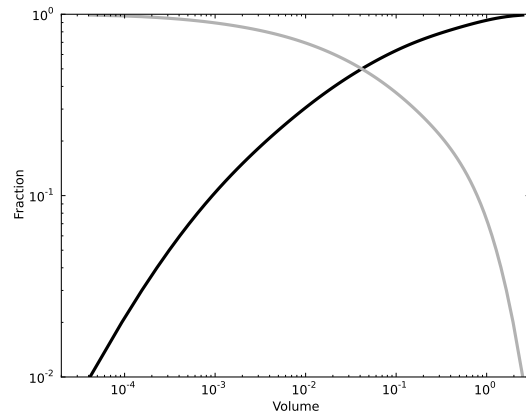


FIG. 8: Bulk of the CDF of the volumes of the tetrahedra in the range from 1% to 99%. The black and gray lines show the CDF,  $F(V)$ , and  $1 - F(V)$  respectively.

The total Eulerian volume  $V_E$  of all tetrahedra grows in the course of evolution

$$V_E = \sum V_i > V_L, \quad (4)$$

where  $V_i$  is the Eulerian volume of the  $i$ -th tetrahedron and the sum is taken over all tetrahedra;  $V_L$  is their total Lagrangian volume. This is not unexpected since many tetrahedra overlap while filling the whole comoving volume – which is equal to the volume of Lagrangian space – without gaps (as can be seen in the two-dimensional illustration in Fig. 1). In the simulation studied here the three-dimensional manifold increased its volume by about 20% compared to its Lagrangian volume.

The cumulative distribution function (CDF) of the volumes of tetrahedra,  $F(V)$  is shown by the black line in Fig. 8, the gray line shows the behavior of  $1 - F(V)$ . This combination allows us to display the behavior of the CDF at small and large values simultaneously, the crossing point marking the median value  $V_{\text{med}} = 0.042h^{-3}\text{Mpc}^3$  (see also Table I for other parameters). In the current simulation, about 30% of the tetrahedra have greater comoving volumes than at the initial time.

### B. Sizes of tetrahedra

We now turn to a simplified characterization of the shapes of tetrahedra using only three size parameters that may be labeled as ‘thickness’, ‘breadth’, and ‘length’ as they satisfy the inequalities  $L > B > T$ . We first select the face with the largest area as the base of the tetrahedron. The height perpendicular to the base is the shortest of all heights, therefore we label it as the thickness  $T$  of the tetrahedron. The shortest height of the base triangle is then labeled as the breadth  $B$ , and finally, the longest edge of the base triangle becomes the length  $L$  of

TABLE I: Statistical characteristics of basic parameters.

	Med.	$\langle \rangle$	std	1% $\leftrightarrow$ 99%	units
Volume	0.042	0.25	0.52	$5 \times 10^{-5} \leftrightarrow 2.0$	$h^{-3} \text{Mpc}^3$
Thickness	0.14	0.27	0.33	$2 \times 10^{-3} \leftrightarrow 1.4$	$h^{-1} \text{Mpc}$
Breadth	0.74	0.94	0.72	$8 \times 10^{-2} \leftrightarrow 2.8$	$h^{-1} \text{Mpc}$
Length	2.88	2.88	1.58	$2 \times 10^{-1} \leftrightarrow 6.9$	$h^{-1} \text{Mpc}$

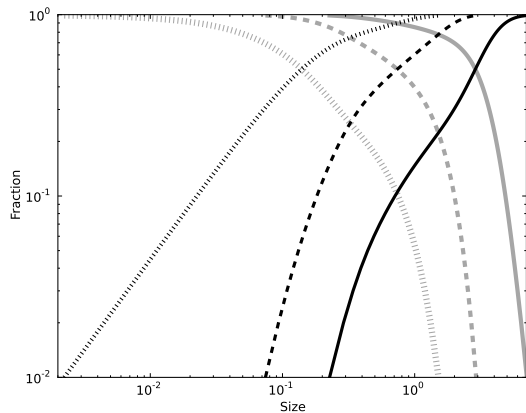


FIG. 9: CDFs  $F(T)$ ,  $F(B)$  and  $F(L)$  are shown as the black dotted, dashed and solid lines respectively. The corresponding gray lines represent  $1 - F$  for each size parameter.

the tetrahedron. The volume of the tetrahedron can be expressed in terms of  $L, B, T$  as  $V = 1/6 L B T$ .

The cumulative distribution functions of the basic tetrahedra sizes – the lengths, breadths, and thicknesses – are shown in Fig. 9. The median, mean and standard deviation of these parameters are given in Table 1 (the volumes are in units of  $h^{-3} \text{Mpc}^3$  and lengths in units of  $h^{-1} \text{Mpc}$ ). Some tetrahedra at the final stage have greater comoving sizes than at the initial time: 17%, 34% and 80% of tetrahedra have greater thickness,  $T$ , or breadth,  $B$ , or length,  $L$  respectively. Table I provides also the range of the distribution between 1% of the lowest and 1% of the highest values.

### C. Cross-correlations between the tetrahedra basic parameters

The basic geometrical parameters of the tetrahedra characterizing their sizes and shapes i.e., the volume, thickness, breadth, and length are obviously not statistically independent. Table 1 shows the cross-correlation coefficients ( $C(P_i, P_j)$ ) between parameters  $P_i$  and  $P_j$ , where  $P_i = V, T, B$ , or  $L$ . Although their distribution functions are not Gaussian as demonstrated by Figs. 8 and 9, these numbers provide a certain sense of statistical dependence between the parameters.

Despite the fact that the length, breadth, and thickness of a tetrahedron enter the expression for the vol-

TABLE II: Cross-correlations between basic parameters.

	Thickness	Breadth	Length
Volume	0.88	0.67	0.38
Thickness		0.61	0.31
Breadth			0.52

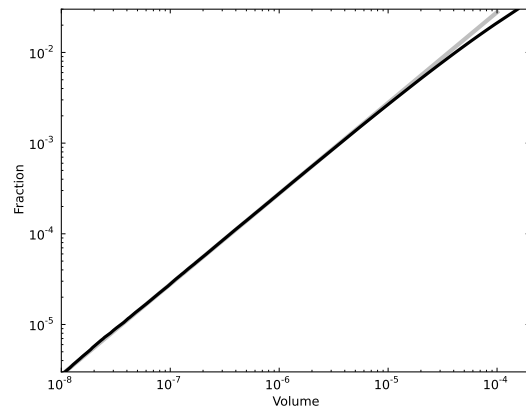


FIG. 10: CDF,  $F(V)$ , of 3% of the least voluminous tetrahedra. The gray straight line is the power law  $F \propto V$ .

ume in a symmetric manner their statistical roles are quite different, as Table 2 illustrates. The volumes of tetrahedra are much more strongly statistically coupled with the thicknesses ( $C(V, T) = 0.88$ ) than with lengths ( $C(V, L) = 0.38$ ). The coupling of the volumes with breadths is stronger than with the lengths but weaker than with the thicknesses:  $C(V, L) < C(V, B) < C(V, T)$ . The strongest correlation among three sizes of tetrahedra is observed between thickness and breadth and the lowest between thickness and length:  $C(T, L) < C(L, B) < C(T, B)$ .

### D. Low value limit of tetrahedra CDFs

The low value tails are shown in Figs. 10 and 11. The gray straight lines are power laws providing visual guidelines for the shapes of the curves. The slopes of the straight lines are  $n_V = 1$ ,  $n_T = 1$ ,  $n_B = 3.8$  and  $n_L = 6.2$ . The power law approximation works well for the thickness, breadth and volume; it is a little worse for the length but still provides a reasonable description. This behavior shows that the tetrahedra become more anisotropic as their volumes and sizes get smaller.

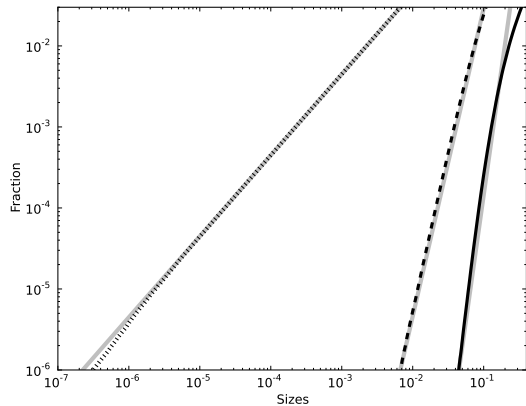


FIG. 11: CDFs,  $F(T)$ ,  $F(B)$ , and  $F(L)$  of the smallest 3% of the corresponding values are shown by the dotted, dashed and solid black lines respectively. The gray solid straight lines show  $F(T) \propto T$ ,  $F(B) \propto B^{3.8}$  and  $F(L) \propto L^{6.2}$  respectively.

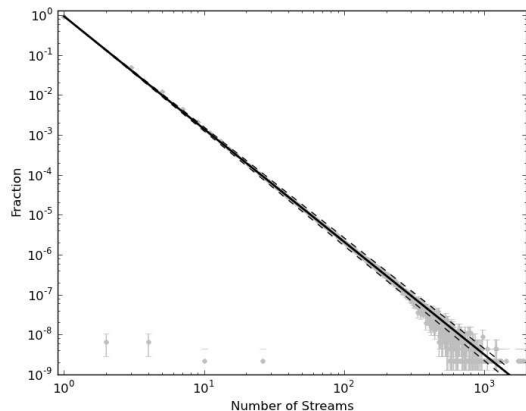


FIG. 12: Fraction of volume as a function of the number of streams. The data points with statistical error bars are shown in gray. The black solid and two dashed lines show the fit  $f_v(n_s) = 0.93 n_s^{-2.82 \pm 0.05}$ .

## VI. MULTI-STREAM AND DENSITY FIELDS

### A. Pdf of the multi-stream field

As mentioned previously, at the lower end of the distance scale, the multi-stream field is defined by the tessellation itself and, in principle, can be computed at an arbitrary number of points, although given a finite particle number, there will be an upper bound beyond which no further useful information is obtained. At the other extreme, one should make sure that the box is large enough to be statistically representative.

The results reported below are for a box size of  $384^3 h^{-1} \text{Mpc}$  with a sampling mesh of size  $768^3$ . (This corresponds roughly to the dynamic range of the under-

TABLE III: Fractions of volume and mass in streams with  $n_s \leq 15$ .

$n_s$	Volume	Mass	$n_s$	Volume	Mass
1	0.929	0.242	3	0.0484	0.169
5	0.0123	0.108	7	$4.47 \times 10^{-3}$	0.0714
9	$2.09 \times 10^{-3}$	0.0500	11	$1.14 \times 10^{-3}$	0.0374
13	$6.96 \times 10^{-4}$	0.0292	15	$4.59 \times 10^{-4}$	0.0234

lying N-body simulation.) The overall statistical parameters of the multi-stream field,  $n_s$ , as determined from this box, are as follows:  $\text{median}(n_s) = 1.0$ ,  $\langle n_s \rangle = 1.27$ ,  $\text{std}(n_s) = 2.2$ .

Figure 12 shows the fractions of volume in the regions as a function of the number of streams. Data points (with statistical error bars) are shown in gray; the black solid line shows the fit

$$f_v(n_s) = 0.93 n_s^{-2.82}, \quad (5)$$

and the dashed lines show the effect of changing the exponent by  $\pm 0.05$ . The pdf has also been estimated by using another set of four cubic boxes of different sizes:  $32$ ,  $64$ ,  $128$  and  $256 h^{-1} \text{Mpc}$  with sampling meshes of variable size. The only difference found was in the high value extent of the pdf: from  $n_s \approx 30$  for the smallest sampling mesh to  $n_s \approx 1000$  for the largest number of sampling points ( $768^3$ ), which is shown in Fig. 12.

Two features of the diagram are worth stressing. First, the data conform remarkably to the simple power law form of Eq. (5). Second, since the number of streams can be only odd (see e.g., Refs. [25, 26]), the very small volume fractions of the regions with even number of streams indicates that the method is numerically robust and errors are negligible. Four spurious data points in the bottom left corner of the figure show the fraction of the volume where the number of streams is even – this occurs in nine instances out of almost a half-billion sampling points.

The fractions of volume occupied by the most voluminous multi-stream flows are given in Table III. The single stream regions provide a simple and robust method for defining voids. Following this definition, we see that voids (defined up to the resolution of the N-body simulation) occupy almost 93% of the simulation volume. This number is somewhat greater than the estimate of  $\sim 86\%$  given in Ref. [19] and is in contradiction with the estimates of  $\sim 17\%$  in Ref. [27] and  $\sim 13\text{--}82\%$  in Ref. [28].

While the definition of the fraction of volume occupied by voids is unambiguously straightforward from the pdf of the multi-stream field alone, the question of other principal morphological types (pancakes/walls, filaments and clumps) is not as simple and requires additional morphological analysis; this analysis will be carried out elsewhere.

## B. Pdf of the density field

The density field has been estimated from the tessellation in the simulation box and with a sampling mesh of the same size as for the multi-stream analysis. The overall statistical parameters of the density field are as follows:  $\text{median}(\rho) = 0.17\bar{\rho}$ ,  $\langle\rho\rangle = 1.008\bar{\rho}$ ,  $\text{std}(\rho) = 28.5\bar{\rho}$ ; since the box in which the analysis is carried out is somewhat smaller than the original simulation box, the mean density is not exactly the mean density of the Universe,  $\bar{\rho}$ . The cross-correlation coefficient of the density and multi-stream fields is 0.45.

Figure 13 shows the number of the sampling mesh nodes,  $N$ , as a function of density computed at that node for a number of different multi-stream flows in the range from one to 151 flows, as well as for the entire density field. The number of mesh nodes,  $N$ , was computed for 32 equal logarithmic bins in the range of densities from  $\rho = 0.01\bar{\rho}$  to  $\rho = 10,000\bar{\rho}$ .

It was stressed in Ref. [15] that although there is a statistical correlation between the multi-stream and density fields, no simple deterministic relation couples them together. This is clearly demonstrated by the results in Fig. 13. As noted for the small box example earlier, with the growth of the number of streams, the average density is shifted to higher values mostly due to a considerable reduction of the number of nodes with low densities. The high value tail of the distribution functions again appears to converge to an approximately limit that (very crudely) can be approximated by a power law  $N \propto \rho^{-1.8}$  which is significantly steeper than it was in the small dense box. The distribution of densities also becomes flatter: the full width at half maximum (FWHM) for the density distribution in the 101-stream flow is about 0.9 on the logarithmic scale, approximately two times greater than that in the three-stream flow.

Figure 14 shows the fraction of mass that resides in the regions with a particular number of streams (dots) and the straight line is the power law

$$f_m = 1.19 n_s^{-1.46}, \quad (6)$$

which provides a good fit to the data points in the range  $5 \leq n_s \lesssim 100$ . Table III provides the list of fractions for several of the most massive multi-stream flows.

The first points in Figs. 12 and 14 (see also the top of Table III) corresponding to one-stream flow are easy to interpret: the voids contain 24% of mass and occupy 93% of volume. The flows with higher number of streams do not correspond to a particular morphology, although there is a general trend of the growth of average density from pancakes to filaments and then to clumps or halos.

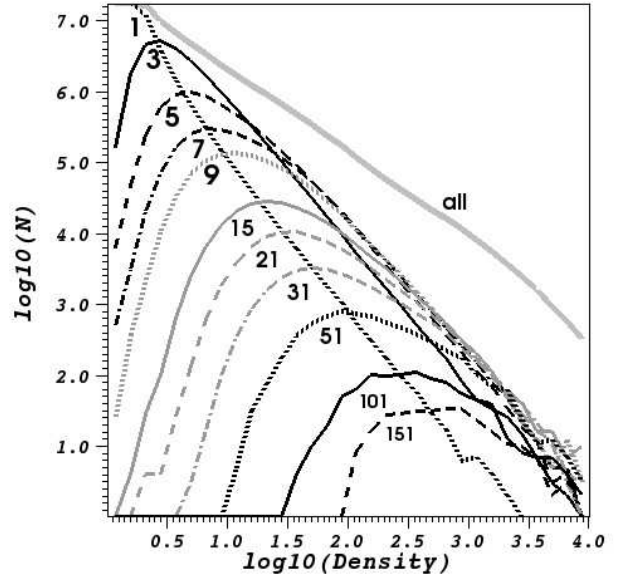


FIG. 13: Number of sampling mesh nodes as a function of density in regions with a fixed number of streams (values shown next to each curve).

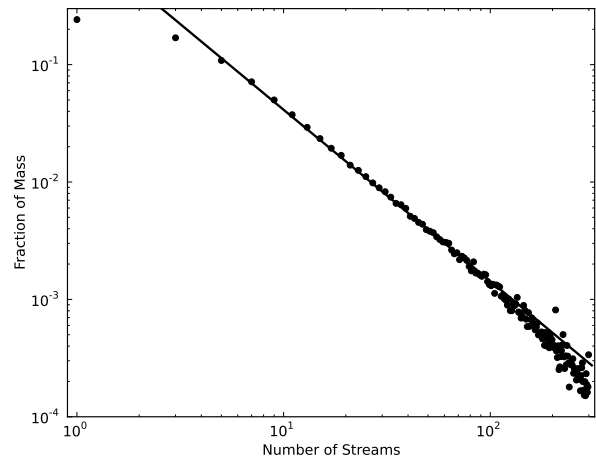


FIG. 14: Fraction of mass as a function of the number of streams is shown by the dots. The solid line is  $F_m = 1.19 n_s^{-1.46}$ .

## VII. COSMOLOGICAL IMPLICATIONS

### A. Voids

Identification of voids in the real Universe and in simulations is not a simple problem for a number of reasons. Setting aside observational issues such as sparse galaxy sampling, projection, and insufficient survey volumes, even in simulations there is no universally accepted

notion of how to best define a void; a good example of the diversity of current practice can be found in Ref. [29].

The multi-stream field provides a unique and simple physical definition of voids as the regions with a one-stream flow (see Ref. [15] for additional discussion). This definition assumes that voids are free from halos that can be resolved by the N-body simulation, therefore it has an inherent small-scale cut-off, interpretable as a cutoff in halo mass. As expected from hierarchical structure formation, simulations with higher mass and force resolution will find that the voids (of lower resolution simulations) are filled with pancakes and filaments at smaller scales. (This can also be seen in a simple way from the adhesion approximation [30].)

The particle mass (or the mass resolution) in the N-body simulation used here is  $m_p \approx 3.6 \times 10^{10} M_\odot$ , therefore the one-stream flow region is free of halos with masses greater than  $\sim 10^{11} - 10^{12} M_\odot$ , since tens of particles are sufficient to find a halo (though not to fully characterize it). The fraction of volume which is free of such halos is about 93% and its total mass fraction is about 24% (Table III). Both numbers are in a good (although not perfect) agreement with the corresponding estimates of Ref. [19] – 86% and 27% respectively.

## B. Sheets/walls (pancakes) and other structures

When the Zel’dovich approximation combined with catastrophe theory was applied to a collisionless medium of weakly interacting particles, a much richer picture than that in the first paper by Zel’dovich [21] emerged [25, 26]. In this picture, the pancakes were just the first multi-stream flows to be formed in accordance with the gravitational instability. The pancakes correspond to a particular kind of singularity emerging at the nonlinear stage; other singularities were associated with filaments and compact clumps. This picture then found further confirmation and development in the adhesion approximation [30, 31].

Ironically, pancakes were not observed in the first three-dimensional simulation of the neutrino dominated universe [18], nor in countless simulations of CDM models of various flavors. Claims of observing pancakes or sheets in cosmological N-body simulations have emerged time after time in the literature, but most of them have been anecdotal. For instance, the authors of Ref. [27] classified more than 45% of volume as occupied by sheets (aka pancakes), which strongly contradicts a visual impression. The authors of Ref. [28] attempted to improve the method used in Ref. [27]; they found that the volume fraction occupied by sheets ranged from 14% to 60% depending on the choice of smoothing scale and other free parameters. Even the lowest value is difficult to reconcile with one’s visual impression. The geometrical analysis based on the evaluation of partial Minkowski functionals revealed that the dark matter density field in an  $\Lambda$ CDM N-body simulation showed a very weak signal of the pres-

ence of pancake-like structures [2]. The result was essentially confirmed by the analysis of the two largest superclusters in another N-body simulation of the  $\Lambda$ CDM cosmology [32] analyzed by a somewhat different method.

However, a new technique, the multiscale morphology filter (MMF) [19] based on the DTFE methodology [1, 3] was able to unambiguously identify walls in  $\Lambda$ CDM N-body simulations. The wall-like structures were found to have the smallest fraction of mass  $f_{m,p}=5.4\%$  and second smallest fraction of volume  $f_{v,p}=4.9\%$  after those for clusters with  $f_{v,c}=0.38\%$ .

If we believe the visual impressions from the study of the small box in this paper then pancakes must be mostly associated with the three-stream flows; this would imply a pancake volume fraction of  $f_{v,p}=4.8\%$  with  $f_{m,p}=17\%$  (see Table III). The former is in agreement with the estimate in Ref. [19] but the latter is more than three times greater than their number.

In a similar fashion, assuming that the filaments are five- and seven-stream flows, we can estimate their volume and mass fractions as  $f_{v,f}=1.6\%$  and  $f_{m,f}=18\%$ , while the estimates of Ref. [19] are  $f_{v,f}=8.8\%$  and  $f_{m,f}=39.2\%$ . Again, there are clear discrepancies. Finally, the numbers for clumps are the remaining  $f_{v,c}=0.7\%$  and  $f_{m,c}=41\%$  by our estimates and  $f_{v,c}=0.38\%$  and  $f_{m,c}=28\%$  by Ref. [19].

We stress that there is an important difference between the pancakes predicted by Zel’dovich and the structures usually called sheets and walls in cosmological studies (see Fig. 5 for an illustration). The Zel’dovich pancakes are defined as three-stream flow regions – as measured in this work – while structures called sheets and walls are always defined as a type of density enhancement, and this was what was measured in Ref. [19]. As we have already stated, there is a positive – but only modest – correlation between density and multi-stream fields, the cross correlation coefficient being 0.45, but there is no one-to-one correspondence, as Figs. 5, 6 and 13 demonstrate. This may well explain the discrepancy, but only a more detailed direct comparison of the two methods can finally resolve the issue.

Comparing the resulting mean overdensities for clumps, filaments, walls/pancakes and voids we find 58.6, 11.2, 3.5 and 0.25 respectively, according to our estimates and 73, 4.45, 1.11 and 0.31 respectively, as found in Ref. [19]. Thus, the method based on using the multi-stream field systematically predicts denser and more compact structures than the method based on the density field, but less dense, and somewhat larger voids.

## C. Caustics

Caustics in the dark matter density field have attracted much attention in recent years because of the potential influence on the (local) experimental detection of dark matter, see e.g., Refs. [33, 34]. However, the study of Ref. [35] has come to the conclusion that the number

of dark matter streams in the vicinity of the sun must be of the order of  $10^{14}$ , which would completely negate the role of caustics. If one assumes this number, the predicted number of streams is absolutely staggering: it means that if the galaxy began to form roughly  $10^{10}$  years ago, the average rate of creation of streams was greater than one per hour. However, the number of the most massive streams contributing half of the mass is  $10^8$  times less, i.e., only about a million streams in the vicinity of the sun.

Our new tessellation method allows us to identify caustic surfaces directly. The caustic surface is the boundary between neighboring fluid elements, one of which has turned inside out one time more than its neighbor. Therefore, if the volumes of the tetrahedra sharing a common face are calculated using Eq. (1) or (3) under the condition that the order of vertices be preserved as it was at the initial stage, then the volumes of the tetrahedra separated by a caustic would have opposite signs. The common face is the element of a caustic surface. The tessellation not only provides an easy way of finding caustic surfaces but also provides the triangulation of the caustic for free. This allows us to compute the partial Minkowski functionals for morphological analysis of the caustics as described in Ref. [2, 32].

Needless to say, the simulation used in this work was not designed for counting numbers of streams in halos that host galaxies such as the Milky Way, with a halo mass of  $\sim 10^{12}M_\odot$ . The mass resolution of the simulation is  $m_p \approx 3.6 \times 10^{10}M_\odot$  and our simulation has been carried out in a completely different regime, where the number of streams reached only about a thousand. Of course one cannot expect to count  $10^{14}$  streams directly simply because the number of particles in the simulations is thousands times less than  $10^{14}$ . However, expecting counts of streams up to a few million and greater in specially designed simulations is quite reasonable.

## VIII. DISCUSSION AND SUMMARY

We have suggested a novel tessellation method for the analysis of structure in the distribution of matter in cosmological N-body simulations. In this initial work, we focused on the relation between density and multi-stream fields. The major features of the method are as follows:

- The method is physically motivated by the fact that the 3-D manifold in 6-D phase space describing the initial state of cold dark matter remains continuous under evolution driven by the gravitational instability.
- The analysis effectively uses the information that is stored in the coordinates of particles and their velocities i.e., the entire phase space information.
- The underlying numerical code is simple and numerically robust.

- The analysis does not involve any free parameters.
- The density and multi-stream fields can be computed with high spatial resolution, limited only by the effective resolution of the underlying particle distribution. This technique can be easily adapted for other scalar, vector or other fields.
- Any field can be computed on an arbitrary regular or point mesh.
- The method allows finding caustic surfaces directly regardless of their shapes.
- In addition, the method immediately provides a triangulation of caustic surfaces that allows for morphological analysis by the evaluation of the full set of partial Minkowski functionals.
- To operate the code requires both initial and final coordinates. If the initial particles are the nodes of a regular mesh then they are obviously not needed. Following the evolution of the system in time is not required, the initial and final coordinates are sufficient for all purposes.

Using the tessellation approach we demonstrated that the structure is considerably more complicated than what can be seen directly in the particle distribution, e.g., by comparing Fig. 3 with Fig. 5; the filaments and pancakes emerge in both multi-stream and density fields as the resolution of the sampling mesh is increased.

The multi-stream and density fields are modestly correlated (the correlation coefficient is 0.45) which is qualitatively reflected in Figs. 6 and 13. Therefore, we confirm the conclusion of Ref. [15], that the multi-stream field provides a considerable amount of new information regarding cosmic structure.

The estimate of the fraction of volume and mass in voids, 93% and 24% respectively, agrees reasonably well with the values of 86% and 27% obtained in Ref. [19]. The Zel'dovich pancakes are undoubtedly present among other generic structures i.e., filaments, clumps and voids in the  $\Lambda$ CDM cosmology which is also in a qualitative agreement with Ref. [19]. However, the preliminary comparison of the volume and mass fractions of the other components of the cosmic web – i.e., pancakes, filaments and clumps – showed serious discrepancies. This is likely due to differences in the definition of (potentially heuristic) quantities such as pancakes, filaments and clumps. Our definitions are based on the multi-stream field, while the definitions used in Ref. [19] are based on the density field. In order to resolve this issue, further morphological analysis is needed. This work is underway and the results will be reported separately.

To the best of our knowledge, the fractions of volume and mass in multi-stream flows are estimated here for the first time. The pdf of volumes demonstrates a remarkable power law scaling over the entire range covering three orders of magnitude in  $n_s$  from one to a thousand (Fig. 12).

The pdf of masses can also be approximated by a power law across most of its range (Fig. 14), though this scaling is not as well fitted as the previous one.

In our approach, the evolution of the system is represented by the evolution of the tetrahedra constructed by the tessellation of Lagrangian space. The tetrahedra represent the major interface between the particle coordinates and all other fields. Their control of the field properties is considerably more elaborate than that of a regular mesh. They also reveal the evolution of the volume elements of dark matter in the gravitational clustering process. Therefore it is interesting to look at their parameters at the final time. We designed three parameters that can be approximately considered as thickness, breadth and length of a tetrahedron. The statistics of these parameters are shown in Fig. 9 and 11 and clearly demonstrate a highly anisotropic character of their deformations at the final time. The voids – where one might expect to find expanding tetrahedra – contain about a quarter of all mass (and therefore about a quarter of

all tetrahedra), however the breadths and lengths of the tetrahedra increased with respect to the initial ones in 34% and 80% cases respectively, which is significantly more than the fraction of the tetrahedra in voids.

The low ends of the CDFs of the tetrahedra volumes and sizes also look like power laws, as shown in Fig. 10 and 11. CDFs of the volumes and thicknesses of the tetrahedra are well approximated by a linear law which means that their pdfs are flat at zero values.

## IX. ACKNOWLEDGMENTS

SH and KH wish to acknowledge the use of supercomputing resources under the Los Alamos National Laboratory Institutional Computing Initiative. We also acknowledge support from the LDRD program at Argonne National Laboratory.

- 
- [1] W.E. Schaap and R. van de Weygaert, *Astron. & Astrophys.* **363**, L29 (2000)
- [2] S.F. Shandarin, J.V. Sheth, and V. Sahni, *MNRAS* **353**, 162 (2004)
- [3] W.E. Schaap, The Delaunay Tessellation Field Estimator, Ph.D. Thesis, The University of Groningen The Netherlands (2007)
- [4] B.J. Ferdosi, H. Buddelmeijer, S.C. Trager, M.H.F. Wilkinson, and J.B.T.M. Roerdink, *Astron. & Astrophys.* **531**, A114 (2011)
- [5] M.J. Way, P.R. Gazis, and J.D. Scargle, *Astrophys. J.* **727**, 48 (2011)
- [6] M. Maciejewski, S. Colombi, V. Springel, C. Alard, and F.R. Bouchet, *MNRAS* **396**, 1329 (2009)
- [7] F.I. Pelupessy, W.E. Schaap, and R. van de Weygaert, *Astron. & Astrophys.* **403**, 389 (2003)
- [8] R.W. Hockney and J.W. Eastwood, *Computer Simulation Using Particles*, IOP Publishing Ltd, Bristol, England (1988)
- [9] R. Gingold and J. Monaghan, *MNRAS* **181**, 375, (1977)
- [10] L.B. Lucy, *Astron. J.* **82**, 1013 (1977)
- [11] I. Arad, A. Dekel, and A. Klypin, *MNRAS* **353**, 15 (2004)
- [12] Y. Ascasibar and J. Binney, *MNRAS* **356**, 872 (2005)
- [13] L.D. Landau and E.M. Lifshitz, *Mechanics*, 3rd. ed., Pergamon Press (1976)
- [14] B. Kuhlman, A.L. Melott, and S.F. Shandarin, *Astrophys. J.* **470**, L41 (1996)
- [15] S.F. Shandarin, *JCAP* **05**, 015 (2011)
- [16] A.G. Doroshkevich, V.S. Ryabenkii, and S.F. Shandarin, *Astrophysics* **9**, 144 (1973)
- [17] A.G. Doroshkevich, E.V. Kotok, A.N. Polyudov, S.F. Shandarin, Yu. S. Sigov, and I.D. Novikov, *MNRAS* **192**, 321(1980)
- [18] A.A. Klypin and S.F. Shandarin, *MNRAS* **204**, 891 (1983)
- [19] M.A. Aragón-Calvo, B.J.T. Jones, R. van de Weygaert, and J.M. van der Hulst, *Astron. & Astrophys.* **474**, 315 (2007)
- [20] E. Platen, R. van de Weygaert, B.J.T. Jones, G. Vegter, and M.A. Aragón Calvo, *MNRAS*, (2011)
- [21] Ya.B. Zel'dovich, *Astron. & Astrophys.* **5**, 84 (1970).
- [22] S.F. Shandarin, A.L. Melott, K. McDavitt, J.L. Pauls, and J. Tinker, *Phys. Rev. Lett.* **75**, 7 (1995)
- [23] S. Habib, et al., *J. Phys. Conf. Ser.* **180** 012019 (2009)
- [24] A. Pope, S. Habib, Z. Lukic, D. Daniel, P. Fasel, N. Desai, and K. Heitmann, *Comp. Sci. Eng.* **12**, 17 (2010)
- [25] V.I. Arnold, S.F. Shandarin, and Ya.B. Zel'dovich, *Geophys. Astrophys. Fluid Dyn.* **20**, 111 (1982).
- [26] S.F. Shandarin and Ya.B. Zel'dovich, *Rev. Mod. Phys.* **61**, 185 (1989).
- [27] O. Hahn, C. Porciani, C.M. Carollo, and A. Dekel, *MNRAS* **375**, 489 (2007)
- [28] J.E. Forero-Romero, Y. Hoffman, S. Gottlöber, A. Klypin, and G. Yepes, *MNRAS* **396**, 1815 (2009)
- [29] J.M. Colberg et al., *MNRAS* **387**, 933 (2008)
- [30] S.N. Gurbatov, A.I. Saichev, and S.F. Shandarin, *MNRAS* **236**, 385 (1989)
- [31] J. Hidding, *Adhesion, a sticky way of understanding Large Scale Structure*, MS Thesis, The University of Groningen, The Netherlands (2010)
- [32] M.A. Aragón-Calvo, S.F. Shandarin, and A. Szalay, arXiv:1006.4178v1 (2010)
- [33] R. Mohayaee and S.F. Shandarin, *MNRAS* **366**, 1217 (2006)
- [34] R. Mohayaee, S.F. Shandarin, and J. Silk, *JCAP* **05**, 015 (2007)
- [35] M. Vogelsberger and S.D.M. White, *MNRAS* **413**, 1419 (2004)
- [36] In this study, two visualization and plotting packages have been used: Mayavi (<http://code.enthought.com/projects/mayavi/>) and VisIt (<https://wci.llnl.gov/codes/visit/>).